Synthesis and Characterization of Silicon Clathrates of type I Na8Si46 and type II NaxSi136 by Thermal Decomposition

Romain Vollondat, Stéphane Roques, Céline Chevalier, Jérémy Bartringer, Jean Luc Rehspringer, Abdelilah Slaoui, Thomas Fix

Synthesis and Characterization of Silicon Clathrates of type I Na_8Si_{46} and type II Na_xSi_{136} by Thermal Decomposition

Romain Vollondat[*1], Stéphane Roques[1], Céline Chevalier[2], Jérémy Bartringer[1], Jean-Luc Rehspringer[3], Abdelilah Slaoui[1], Thomas Fix[1]*

[1] Laboratoire des Sciences de l'Ingénieur, de l'Informatique et de l'Imagerie (ICube), CNRS and University of Strasbourg, 23 rue du Loess, 67037 Strasbourg, France

[2] Université de Lyon; Institut des Nanotechnologies de Lyon INL-UMR5270, CNRS; INSA Lyon; 7 Avenue Jean Capelle, 69621 Villeurbanne, France

[3] Institut de Physique et Chimie des Matériaux de Strasbourg (IPCMS), UMR7504 CNRS and University of Strasbourg, 23 rue du Loess, 67034 Strasbourg, France

Abstract

Type I (Na_8Si_{46}) or type II ($Na_{x\leq 24}Si_{136}$) silicon clathrates films with a large 15 x 45 mm^2 surface have been synthesized from p-type and intrinsic c-Si (001) wafers using a two-step process without the need of any glove box. Conditions to selectively obtain either type I or type II silicon clathrates phase have been finely tuned. Optical absorption coefficients are found much larger in the Si clathrates than in diamond silicon. Type II films provide a direct bandgap of around 1.9 eV which is supporting the high absorption coefficient observed. Photovoltaic response of the films has been confirmed using Surface Photovoltage. As prepared type II films show many surface defects, cracks and inhomogeneities which have been drastically reduced thanks to a pressure annealing treatment.

Keywords: Clathrates compounds, Thermal Decomposition, Intermetallic, Photovoltage, Semiconductors.

*Corresponding author: romain.vollondat@etu.unistra.fr (R.Vollondat, Ph.D. candidate)

1. Introduction

Silicon Clathrates (SiCL) are low-density phases of silicon characterized by their 3D guest-host structure, consisting in an open structure of sp^3 Si-Si bonded polyhedral cages stabilized by the so-called guest atoms which are generally alkali and alkaline earth. First observed for gas hydrates in 1811 [1], the notion of clathrates structures was only introduced in 1945 [2] and such structures were first synthesized for silicon in 1965 [3]. SiCL consist in diverse structures with variable arrangement and size of the cages [4–6]. Two structures are more studied than the others: the type I G_8Si_{24} and the type II $G_{x\leq24}Si_{136}$ SiCL where G is the guest species, usually alkali metals (Li, Na, K, Rb and Cs) [7–10].

The type I structure is identified by the assembly of two small Si_{20} (also noted 5^{12}) and six Si_{24} ($5^{12}6^2$) cages, which are each filled by a guest atom. The type II structure is made of sixteen small Si_{20} (5^{12}) cages and eight large Si_{28} ($5^{12}6^4$) cages with the ability of its guest atoms to be either removed [11] or inserted [12] up to an occupation value of x=30.5 [13] under high pressure synthesis. Extensive research has been led on the group IV clathrates [14] with various guests and even ternary [15] and quaternary [16] SiCL where the framework and the guest are both formed by two or more different chemical species.

The main focus on SiCL has been for a long time in thermoelectric applications [17,18] thanks to the rattling of the guest atoms [19] inside the cages. Interest into optoelectronic applications [20–23] started after theoretical studies hinted that guest free SiCL would exhibit an indirect band-gap of 1.8 eV for the type I [24] but a direct band-gap for 1.9 eV for the type II [25,26]. In particular, the direct band-gap of the type II could offer an alternative to the diamond silicon widely used in microelectronics that has an indirect band-gap of 1.1 eV and thus poor light-absorption in the visible range [27]. They are now also considered as candidates for applications as anodes in batteries [28,29].

To reach optoelectronic devices, a synthesis pathway was needed to obtain SiCL in the form of films as most of the previous studies were based on powders or monocrystals. Such film synthesis has been recently reported using the thermal decomposition pathway [21,30–34]. The latter relies on a two-step process starting with the formation of a sodium

silicide Zintl phase Na_4Si_4 by the reaction of silicon with sodium vapor, followed by the decomposition of this precursor into the desired SiCL type I (SiCL-I) and type II (SiCL-II) structure. In this work, we report on our optimized conditions to obtain selectively SiCL-I or SiCL-II films on silicon substrates, and we investigate their optical, electrical and optoelectronic properties.

2. Experimental

Fig. 1 displays the photographs of the different apparatus used for the two step-process of thermal decomposition. The fabrication method is similar to previously reported method [30,35] used to prepare Na_xSi_{136} film on silicon wafer adapted from the preparation route of SiCL powder [36,37]. The precursor film of Zintl phase is obtained as follows: a sodium slice with a mass of around 0.2g is cut from a sodium ingot (99.8% purity, Alfa Aesar, CAS #7440-23-5) and is immediately placed in a sealed off recipient filled with cyclohexane (99+% purity, Alfa Aesar, CAS #110-82-7) to prevent the oxidation of the metallic sodium. The sodium and cyclohexane are handled following safety precautions. A 525 ±25 µm thick silicon wafer (c-Si (001)) cut into a rectangular 54 x 37 mm² shape is

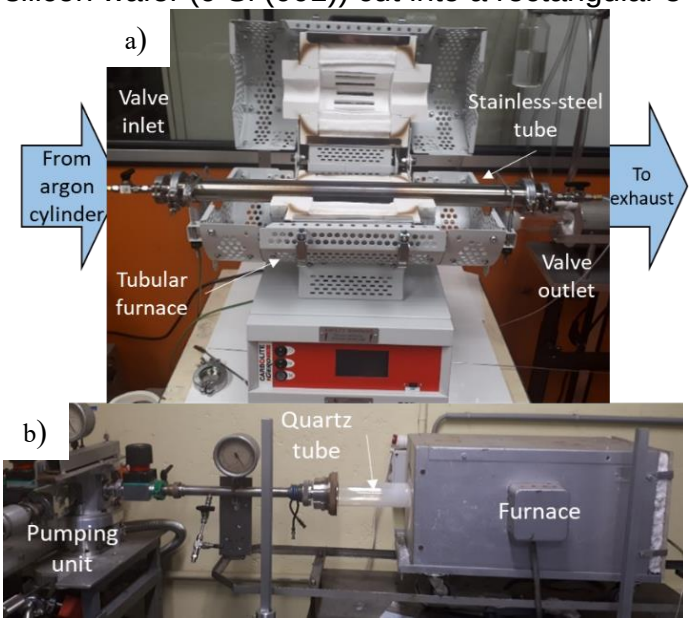

Fig. 1. Photographs of the experimental setup used for a) the synthesis of the Zintl precursor film b) for the thermal decomposition of the precursor into the silicon clathrates film.

treated with HF (10% vol) for 2 minutes. The Si wafers are either p-type with a resistivity of 1-5 Ω·cm or intrinsic with a resistivity >10 kΩ·cm. Right after the cleaning of the Si wafer, the sodium slice is placed in the middle of an Inconel boat (54 x 18 x 13.3 mm^3, ANALAB, ref. AR9001). The boat is quickly covered with the silicon wafer, as shown in the schematic view of Fig. S1 in the Supplementary Information (SI). The system {Boat + Sodium slice + Si Wafer} along with a tantalum coiled wire, put here to catch any leftover traces of oxygen, is inserted in the middle of a stainless-steel tube (diameter 45mm, length 65cm, Inox SST304, Hositrad KF40 Full Nipple), itself placed into a tubular furnace (Fig. 1a). Argon (99.9999+%) is flown in the tube at $1.6x10^5$ Pa and maintained for 10 minutes after closing the open flange of the stainless-steel tube. It is then heated at a temperature between 570 and 630°C with a ramp of 5°C/min and a dwell time of 13 to 19h. The tube is then naturally cooled down to room temperature and flushed again with Ar for 10 minutes. The Si wafer covered with the Zintl phase film is pulled out and immediately put in a quartz tube to reach a dynamic vacuum of $4.5x10^{-5}$ Pa to limit any possible reaction between the Na_4Si_4 with the ambient humidity (Fig. 1b). As opposed to prior authors [21,30,35], no stainless-steal container is used to keep the NaSi film completely safe from the ambient humidity. Once the vacuum is achieved, a furnace is wrapped around the quartz tube, heated to 400°C with a ramp of 10°C/min and a duration from 3h to 24h under dynamic vacuum, and then let to naturally cool down to room temperature. The sample is then pulled out of the tube and cleaned with ethanol then deionized water to remove any excess sodium. Once no bubbling from the surface of the film is witnessed, the sample can be removed and blow-dried for further treatments or characterizations. Photograph of the obtained sample is available in Fig. S2 along with SEM surface observations of both SiCL.

Two samples cut into four smaller 1.5 x 1.5 cm^2 pieces were submitted to press annealing in air at temperatures of 200°C and 250°C with applied forces of 2 kN and 4 kN (8.9 MPa and 17.8 MPa respectively) using a Rondol hydraulic press equipped with two heating steel plates.

X-ray diffraction (XRD) is performed with a Bruker D8 DISCOVER with a Cu $K_{\alpha 1}$ wavelength of 0.154056 nm. The Jana2006 software has been used to refine the lattice

parameters. Scanning electron microscopy (SEM) images were obtained thanks to both a JEOL 6700F and a Zeiss GeminiSEM 500 with a field-emission gun (FEG), operating respectively at 3 kV and 5 kV in the SE In-Lense mode instrument. Energy Dispersive X-ray Spectroscopy (EDS) was used to estimate the composition of the material in different positions in the films. Transmission electron microscopy (TEM) was performed with a Topcon 002B (200kV, EDX, CCD camera). Raman spectroscopy and Photoluminescence (PL) are measured at 293 K using a JOBIN YVON LabRam Aramis apparatus with a 532nm laser. Spectroscopic Ellipsometry was performed using a HORIBA Uvisel Lt M200 FGMS (210-880nm). Current-voltage (IV) characteristics were measured using an Orial VeraSol-2 AAA Solar Simulator in AM 1.5G conditions at room temperature coupled with a Keithley 2461 SourceMeter. Kelvin Probe (KP) and Surface PhotoVoltage (SPV) measurements were performed with a single point Kelvin Probe system (KP Technology KP020) with a 2 mm diameter gold tip, and using either a halogen source with calibrated illumination for white light SPV or a GR50-605 (Thorlabs) monochromator of 600 g/mm^{-1} grating for spectroscopic SPV mode.

3. Results and discussion

Fig. 2 indicates the phases present in the films depending on the first annealing temperature. SiCL-I films are reproducibly obtained at a temperature of 630°C for the precursor formation step, with minor SiCL-II and diamond silicon phases as reported in Fig. 3a. with a 10.1954 Å lattice parameter. Pure SiCL-II films are obtained for a lower temperature of 600°C and no parasitic phases are detected by XRD as shown in Fig. 3b. The lattice parameter of these SiCL-II films varies according to the duration of the thermal decomposition annealing step. For the routine 3h duration, it gives a reproducible value of 1,46378 nm, corresponding to an occupation x of ~7 (Na_7Si_{136}) obtained by Rietveld refinement. Minor impurities fitting with $NaSi_6$ [38] was observed in some films. The impact of the temperature on the nature of the film during the precursor formation step can be explained by the increase of the sodium vapor pressure with temperature [39]. For temperature above 610°C in our setup, a metallic sodium layer is observed on top of the Na_4Si_4 film, supposedly due to the cooling process, and is more and more continuous as the temperature increases. For a 630°C temperature, the whole Na_4Si_4 film is covered by

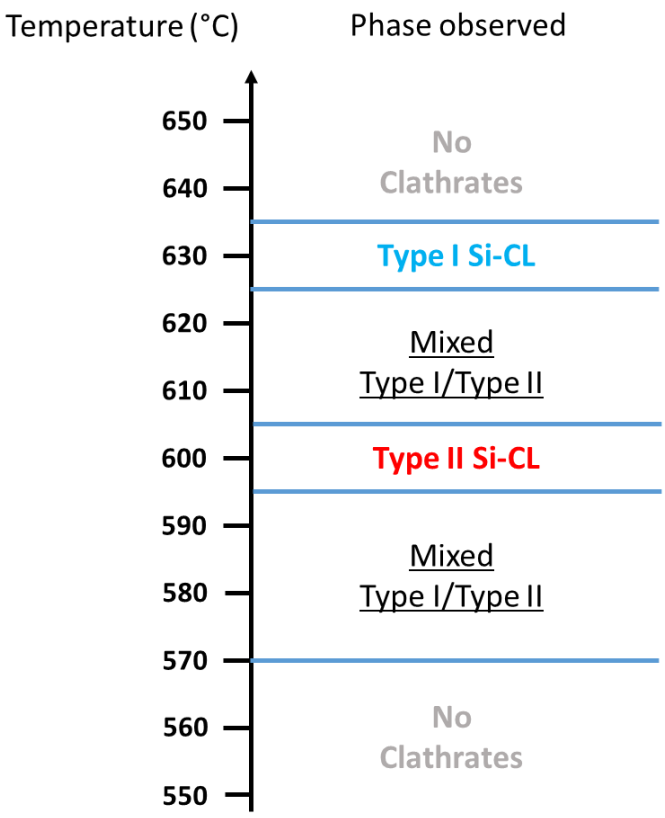

Fig. 2. Nature of the films obtained depending on the temperature of the first annealing step.

this sodium layer. As reported in a previous study [40], the sodium vapor is a crucial parameter during the thermal decomposition step to determine which of the SiCL-I or SiCL-II type will prevail or coexist. As the Na_4Si_4 film at 630°C is covered by excess sodium in contrast to the 600°C one where no trace of metallic sodium is observed, this excess sodium will favor the type I SiCL formation over the type II. For temperature below 600°C, the obtained samples exhibit no continuous films across the sample, hinting toward a lack of sodium as reactant. However, in contrast to groups avoiding any contact of the NaSi film with air [32], reducing the duration of the thermal decomposition annealing did not lead to thinner films. An annealing of a least 13h is required to obtain a SiCL film. This could be the main drawback of operating this thermal decomposition process with no glove box as it is thought that during the very short exposure of air during the transfer of the sample a too thin Na_4Si_4 film exposed to air could be instantly degraded by the humidity as Na_4Si_4 is known to react with water.

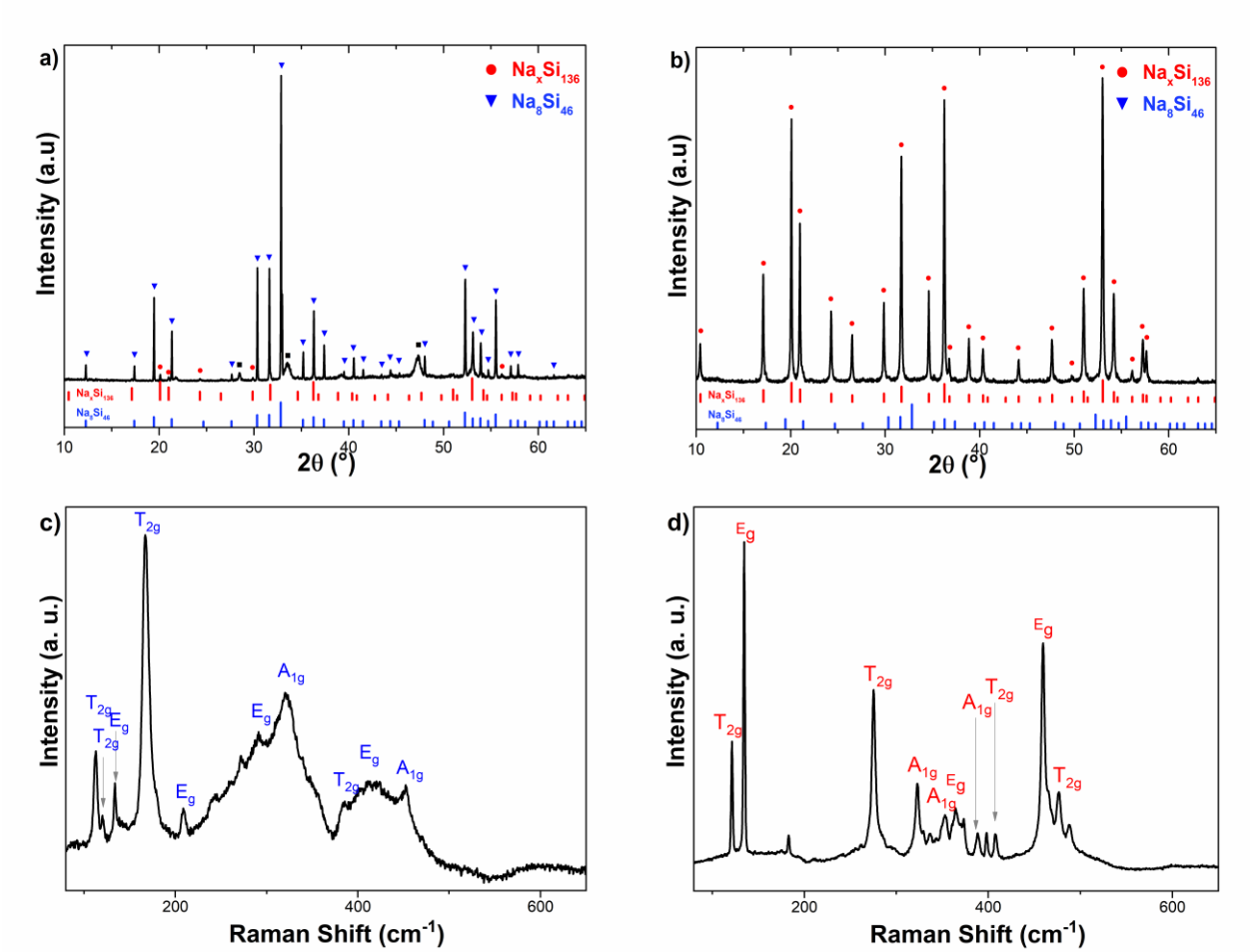

Fig. 3. XRD patterns for the a) SiCL-I b) SiCL-II films. The red cercles refers to Na_1Si_{136} (JCPDS 01-089-5535), the blue triangles to Na_8Si_{46} (JCPDS 01-089-5534) and the black squares to diamond Silicon (JCPDS 00-027-1402). Raman spectra obtained with a 532nm laser at 1.1 mW using a 2400 $g.mm^{-1}$ grating with a 50 µm slit for c) SiCL-I d) SiCL-II films.

Fig. 3c shows the Raman spectrum related to the SiCL-I films. Since Na_8Si_{46} has a metallic character, the broadness of the detected vibrations peaks is important. Still, the observed vibration shifts are in agreements with previous theoretical and experimental studies [41–43]. Fig. 3d depicts the SiCL-II film Raman vibrations which are also similar to previous calculations [44] and experiments [45]. The peaks for the SiCL-II films are much easier to detect and reproducible across the surface than the SiCL-I phase. The well-defined profile of the peaks is coherent with the estimated occupation that would give semiconducting SiCL-II. Indeed, it has been showed that for sodium occupation higher than x=8, SiCL-II presents a metallic character and the related Raman peaks are broader

[46]. It also important to warn that both SiCL-I and SiCL-II are degraded by long and/or repeated exposition to the laser at power above 2 mW The resulting spectrum gives a sole peak slightly before 500 cm^{-1}, hinting toward the transformation into an amorphous silicon phase. Electrical measurements were performed on SiCL-I and SiCL-II films prepared from intrinsic silicon substrates (c-Si (001)). As expected, the SiCL-II films grown are semi-conducting and show a resistivity of 5.2 Ω·cm, a mobility of 70 $cm^2V^{-1}s^{-1}$, and a n-type behavior, as reported in previous studies [45], but with low carrier concentration of $5x10^{16}$ cm^{-3}. In opposition the SiCL-I film has a metallic character, also reported in [46], with a resistivity of 1.1 x 10^{-3} Ω·cm for a mobility of 1.3 x 10^3 $cm^2V^{-1}s^{-1}$ with a carrier concentration of $9.5x10^{16}$ cm^{-3}.

Optical properties such as absorption coefficient, extinction coefficient and refractive (see Fig. S4) index of the two types of SiCL films were investigated using spectroscopic ellipsometry under the assumption that no light will transmit through the 30 µm thick SiCL-I or SiCL-II films, which is very reasonable according to previous measurements of absorption coefficient by transmission in SiCL thin films 23,41. Fig. 4a reports the absorption coefficient obtained. For the SiCL-II films, the estimated values and behavior are in agreement with previously determined value obtained by UV-Visible measurement on thin film deposited on sapphire [21,47] or others methods [37]. The SiCL-I film is even more able to absorb light and the absorption coefficient is rising continuously as the photon energy increases to reach $6.7x10^5$ cm^{-1} at 4.5 eV. In both cases, the SiCL films are better light absorber than diamond silicon [27] in the whole visible light range down to the near infrared with α in the 10^5 cm^{-1} order of magnitude for SiCL-I and 10^4 for SiCL-II. The measurements exhibit high noise to signal ratio because of the low reflectivity of both

types of SiCL and the roughness of the surface due to the sublimation step of the sodium during the annealing under dynamic vacuum.

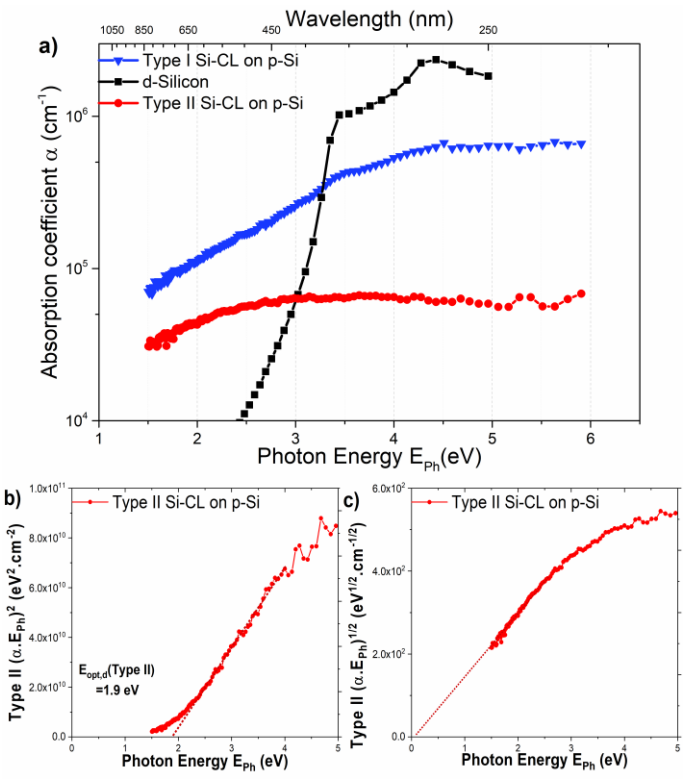

Fig. 4. a) Absorption coefficients α of the SiCL films and Silicon versus the photon energy E_{Ph} in the 210-800 nm range. b) Tauc Plot for SiCL-II film assuming a b) direct c) indirect optical band gap.

Tauc plots were plotted for SiCL-II films for both direct $(\alpha . E_{ph})^2$ vs. E_{Ph} or indirect $(\alpha . E_{ph})^{\frac{1}{2}}$ vs. E_{Ph} band gap (Fig. 4b and 4c). Tauc plot for SiCL-I film were not drawn due to its metallic character. An optical direct band gap at around 1.9 eV is obtained for the SiCL-II film with no sign of optical indirect bandgap. The photoluminescence was also investigated and gave out a broad peak centered at 1.75 eV (Fig. S2), which is coherent with previous observations [14,48]. This broad peak is thought to originate from the very distraught state of the film, both in surface and in the bulk but could also be due to a sodium-rich silicon disordered phase, as it will be discussed from the SEM observations.

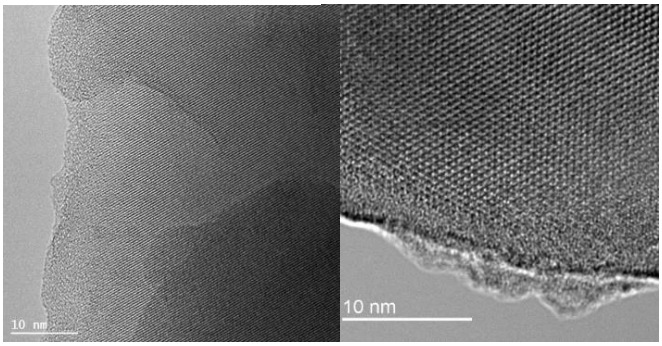

Fig. 5. TEM observations of SiCL-I (on the left) and SiCL-II (on the right) from a suspension in ethanol.

TEM observations were also possible by gently scratching some of the SiCL films and grinding into a thin powder using a ceramic mortar. This powder is then put on a membrane using a suspension in ethanol. TEM pictures gave out the view of large nicely crystalized area of about 60 nm long as seen in Fig. 5. The crystallite size observed by TEM is matching the one estimated by XRD analysis (55 nm for SiCL-I, 53 nm for SiCL-II). While the bulk of the grain is crystalline, a disordered phase made of silicon is observed around the border. This disordered phase has already been reported by EPR measurements [49,50] and could be due to an amorphous phase [51] formed at the surface of SiCL. Several orientations of the type II phase were observed as reported in Fig. S5. Some impurities from diamond silicon were also spotted for the type I sample. EDX measurements (Fig. S6) indicate a $Na_{1.9}Si_{136}$ (1.37% atomic percentage in sodium) composition for the SiCL-II and give a 13.9% atomic percentage of sodium for the SiCL-I slightly lower than the expected 14.8%, which could be explained by diamond silicon impurities.

The films were further investigated using Surface Photovoltage (SPV) thanks to a Kelvin Probe apparatus coupled either to white light with controlled intensity (transient SPV

and SPV vs. intensity) or light delivered by a monochromator (surface photovoltage spectroscopy SPS).

Fig. 6a shows the measured contact potential difference (CPD) vs. time, for SiCL-I and SiCL-II grown on a p-doped Si substrate, during dark/light cycles with the white light at

full intensity. For both SiCL-I and SiCL-II samples, a change in the value of the CPD is observed during the cycles, which means both materials have a photovoltaic response. The CPD(light) is higher than the CPD(dark) for the type I sample, which is probably caused by the p-type substrate underneath as measured in Fig. S7, because type I is not

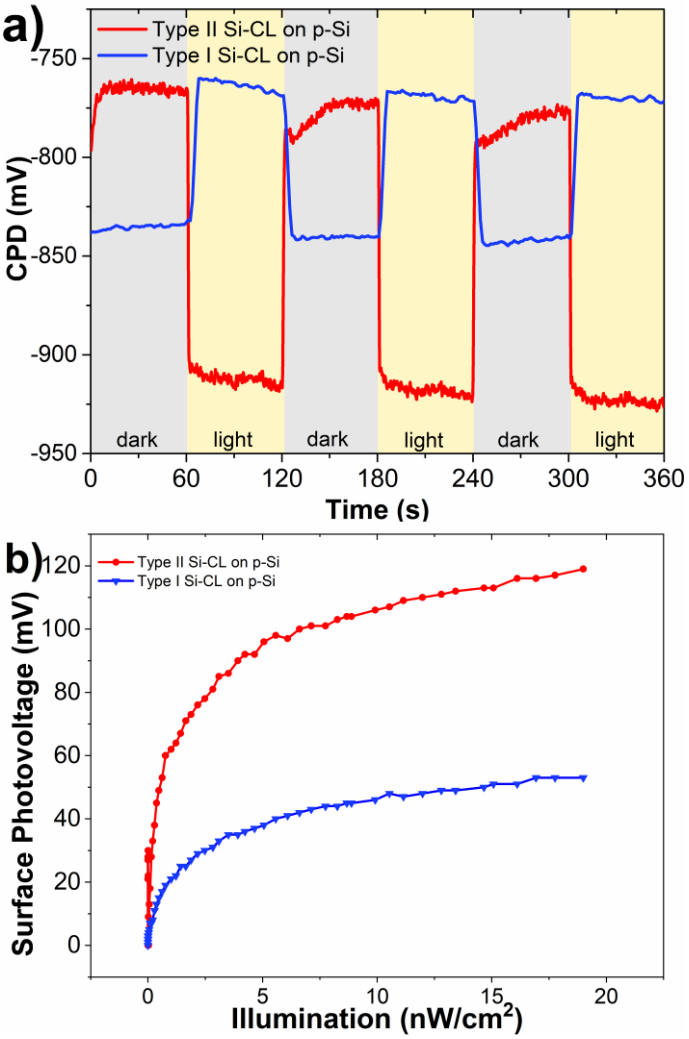

Fig. 6. a) Variation of the Contact Potential Difference (CPD) measured on the Silicon Clathrates samples during cycle between illumination by halogen visible light and dark. b) Surface Photovoltage (SPV) of the Silicon Clathrates samples according to the illumination delivered by the halogen visible light.

supposed to be a semiconductor but a metal. In contrast, the type II shows an opposite variation of CPD with light, which is the evolution expected for n-type carriers, as already observed by Hall effect. The fast responses observed may indicate a short lifetime of the photocarriers generated during the illumination of the materials [52].

Next the SPV signal was measured vs. white light intensity following the formula $SPV(Illumination) = |CPD(Illumination) - CPD_{dark}|$ as shown in Fig. 6b. The SPV signal is gradually increasing following a logarithmic increase as expected for a semiconductor and reaches a non-saturated value of 50 mV and 120 mV for type I and II respectively at the maximum illumination of 19 nW/cm².

This is compared to a quickly reached 400 eV-saturated value at the same maximum illumination for the p-doped Si substrate (Fig. S8). IV measurements done on the s-II film allow to roughly reach a short-circuit current density J_{SC} of about 3 nA/cm^{-2} while the open-circuit voltage V_{OC} value of 95 mV is close to the SPV obtained previously. We linked the extremely low value of J_{SC} obtained to the inhomogeneous state of the s-II film and its fragile adherence to the silicon substrate.

To summarise the last two experiments, both type of samples are photoactive. SiCL-I displays a p-type behaviour originating from the substrate while SiCL-II provides a n-type behaviour. Nothing is known about the origin of the photocarriers that are observed. While early solar cells based on Si-CL were proposed in previous studies [22,33], the low short-circuit currents measured did not allow to measure external quantum efficiency EQE and therefore a doubt was present as to whether the photocarriers observed were generated by SiCL or by diamond Si impurities. In this way the optoelectronic properties of the films were further investigated using SPS. The SPV values obtained from the CPD were normalized by the photon flux at to each wavelength delivered by the monochromator. The SPS curve obtained for p-doped Silicon is very similar to the profile obtained by EQE as it can be seen in Fig. 7. For the SiCL films, as the SPV signal is lower than for p-type Silicon, the SPS signal is noisier but still accessible. It can be observed in Fig. 7 that the behavior of the SiCL SPS signal is completely different from the one of p-type Si. The SPS signal of SiCL-I is very weak with a maximum in the 450-550 nm range. The signal is quite low and thus it is difficult to extract valuable information from the background

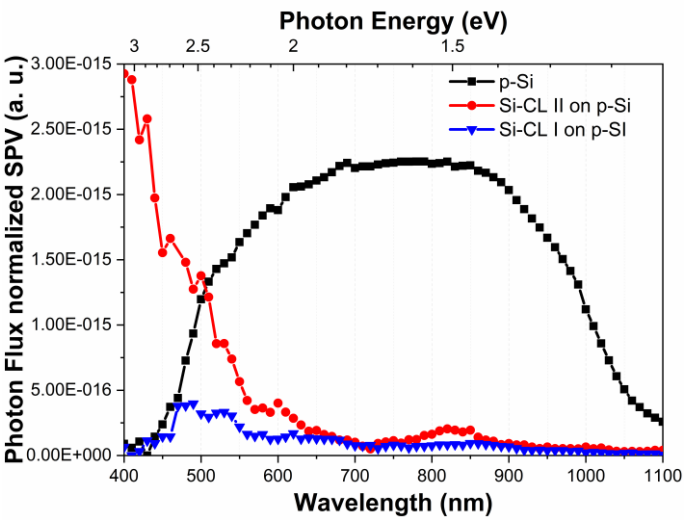

Fig. 7. Surface Photovoltage Spectroscopy of the Silicon Clathrates samples and Silicon by normalizing the SPV by the photon flux versus the wavelength of the light.

noise. In opposition the SPS signal of SiCL-II is very intense at 400 nm and gradually goes down from 400 to 650 nm. It is nearly zero above 650 nm which is in agreement with the bandgap of 1.9 eV measured from Tauc plot and photoluminescence. This clearly proves that the photocarriers generated in SiCL-II films do not originate from diamond Si but from the type II silicon clathrates themselves with a bandgap of around 1.9 eV.

In our previous work, press annealing has been beneficial to the Type I Silicon Clathrates morphology [33]. Here we investigate the effect of this technique on the Type II films. Two SiCL-II films with very rough surfaces were press annealed at 200 and 250°C with forces of 2 and 4 kN for 30 minutes. In contrast to what has been observed for type-I films, the type-II films obtained in this work were neither able to be compacted nor re-oriented in a significant way. Still, the beneficial impact is a smoothed surface as shown in Fig. S9. It was expected that, as the type II structure is less dense than type I and the SiCL-II samples surface is more fractured than the SiCL-I, a contraction of the films would be observed. In contrast the experimental results show that the contraction and re-orientation of SiCL-I samples may be mainly due to inferior thermal stability of the type I compared to the type II structure [36]. Still, the annealing under pressure of the type-II films offers a

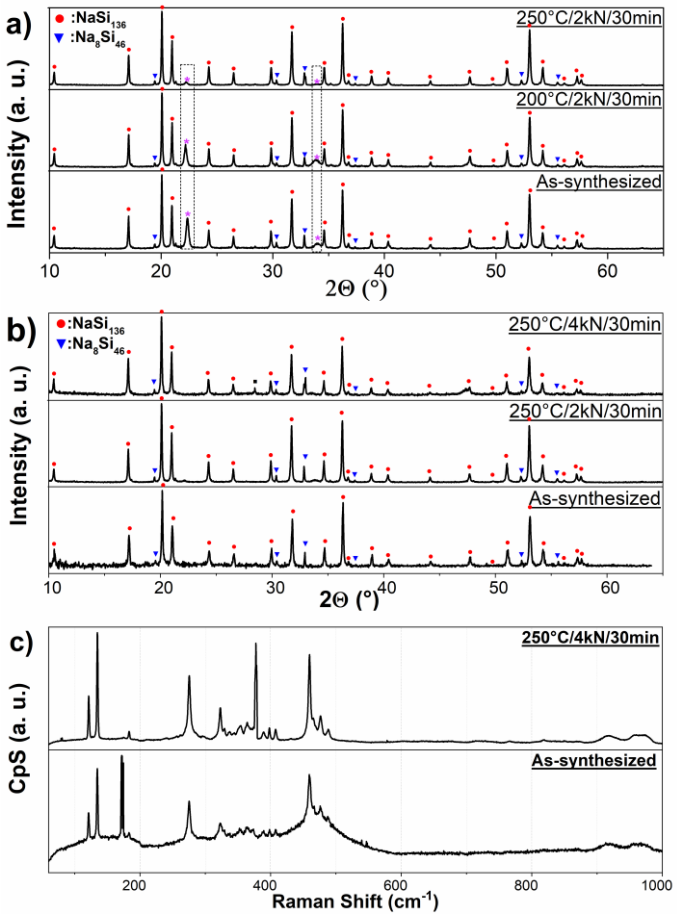

Fig. 8. XRD patterns for the a) SiCL-II films submitted to 200°C and 250°C with a force of 2kN b) SiCL-II films submitted to 2 and 4 kN at a temperature of 250°C. Purple asterisks are for the $NaSi_6$ (JCPDS 04-020-2170) c) Raman Spectra obtained with a 532nm laser before and after press annealing of a SiCL-II sample at 250°C for a force of 4 kN during 30 minutes.

safe way to purify type-II sample as show in Fig. 8a, where the $NaSi_6$ impurities observed reflections are gradually losing intensity as the temperature of the press annealing is increasing. Fig. 8b. reports that for 250°C, as the applied force increases, the sodium occupation is slightly reduced. This does not forcefully mean that the press annealing allows the removal of the sodium guest atoms from the cages but rather that the thickness

of the normally observed sodium-rich crust observed at the surface of the SiCL-II films is gradually reduced as it can be seen in Fig. S10.

We have not yet determined whether this crust is another disordered and more porous Na-Si phase or a badly crystallized sodium riche type-II Silicon Clathrates. The reduction of the thickness of this sodium-rich crust is also supported by the Raman spectra reported in Fig. 8c. For the rough as-synthesized SiCL-II sample the Raman peaks are drowned in a broad envelope for shifts between 75 to 480 cm^{-1}. But this envelope has disappeared after the press annealing process at 250°C for 4 kN force for 30 minutes. This could mean that the envelope signal is originating from the sodium-rich crust at the surface of those samples. Hall effect measurement on these samples give a resistivity of 10 Ω·cm and a mobility of 65 $cm^2V^{-1}s^{-1}$ before any treatment and shift to 300 Ω·cm and 48 $cm^2V^{-1}s^{-1}$ after press annealing. This could confirm the sublimation of a few sodium atoms from the SiCL cages during the process. However, annealing under pressure only slightly impact the absorption coefficient and the surface photovoltage as depicted in Fig. S11.

4. Conclusion

The experimental conditions to selectively obtain Type I or Type II Silicon Clathrates have been determined and reported for our specific setup which does not need any glove box. SiCL-I and SiCL-II phases were synthesized on both p-doped an intrinsic silicon wafers and structural, optical, electrical and photovoltaic properties were characterized. Type II Silicon Clathrates synthesized this way have low sodium occupancy of around 7 and thus are semi-conducting material while Type I has a metallic behavior. A sodium-rich crust at the very surface of the Silicon Clathrates films has been observed thanks to SEM and linked to its plausible Raman signature. Press annealing impact was found to differ depending on the Silicon Clathrates type but still allow smoother surfaces. It represents a pathway to improve morphology of the Type-II Silicon Clathrates and therefore to further improve the photovoltaic properties and solar cell efficiencies. In addition to this, composition homogeneity of the films should be improved by a better comprehension of the thermal decomposition process.

Still, the optical, electrical, SPV and SPS study in this work unambiguously demonstrates that photocarriers are generated and mobile in the SiCL-II material, with a direct bandgap of around 1.9 eV and a mobility reaching 70 $cm^2V^{-1}s^{-1}$. This result paves the way for optoelectronic applications based on semiconducting silicon clathrates and is a further source of stimulation for this field of research.

Author Contribution

R. Vollondat: Conceptualization, Investigation, Methodology, Writing – original draft. **S. Roques:** Investigation. **C. Chevalier:** Investigation. **J. Bartringer:** Investigation. **J-L Rehspringer:** Methodology. **A. Slaoui:** Conceptualization, Project Administration. **T. Fix:** Conceptualization, Project Administration, Writing – review & editing.

Conflict of interest

There are no conflicts to declare.

Acknowledgments

We thank N. Zimmermann for technical assistance, C. Leuvrey and J. Faerber for SEM observations performed at the MEB-CRO platform and C. Bouillet for observations and measurements at the TEM platform of the IPCMS. This project has received financial support from the CNRS through the 80|Prime program and through the MITI interdisciplinary programs.

Appendix A. Supporting information

Supporting Information: Additional experimental details and optical properties measurement on the samples and on a diamond silicon reference along with SEM and TEM views including EDX analysis.

References

[1] H. Davy, VIII. On a combination of oxymuriatic gas and oxygene gas, Phil. Trans. R. Soc. 101 (1811) 155–162. https://doi.org/10.1098/rstl.1811.0008.

[2] H.M. Powell, 15. The structure of molecular compounds. Part IV. Clathrate compounds, J. Chem. Soc. (1948) 61. https://doi.org/10.1039/jr9480000061.

[3] J.S. Kasper, P. Hagenmuller, M. Pouchard, C. Cros, Clathrate Structure of Silicon Na_8Si_{46} and Na_xSi_{136} ($x < 11$), Science. 150 (1965) 1713–1714. https://doi.org/10.1126/science.150.3704.1713.

[4] L. Krishna, C.A. Koh, Inorganic and methane clathrates: Versatility of guest–host compounds for energy harvesting, MRS Energy & Sustainability. 2 (2015) 8. https://doi.org/10.1557/mre.2015.9.

[5] G.S. Nolas, ed., The Physics and Chemistry of Inorganic Clathrates, Springer Netherlands, Dordrecht, 2014. https://doi.org/10.1007/978-94-017-9127-4.

[6] E.D. Sloan, C.A. Koh, Clathrate hydrates of natural gases, 3rd ed, CRC Press, Boca Raton, FL, 2008.

[7] I. Veremchuk, M. Beekman, I. Antonyshyn, W. Schnelle, M. Baitinger, G. Nolas, Y. Grin, Binary Alkali-Metal Silicon Clathrates by Spark Plasma Sintering: Preparation and Characterization, Materials. 9 (2016) 593. https://doi.org/10.3390/ma9070593.

[8] C. Cros, M. Pouchard, P. Hagenmuller, Sur une nouvelle famille de clathrates minéraux isotypes des hydrates de gaz et de liquides. Interprétation des résultats obtenus, Journal of Solid State Chemistry. 2 (1970) 570–581. https://doi.org/10.1016/0022-4596(70)90053-8.

[9] T. Kume, T. Koda, S. Sasaki, H. Shimizu, J.S. Tse, High-pressure Raman study of the potassium-doped silicon clathrate K8Si46, Phys. Rev. B. 70 (2004) 052101. https://doi.org/10.1103/PhysRevB.70.052101.

[10] B. Böhme, M. Bobnar, A. Ormeci, S. Peters, W. Schnelle, M. Baitinger, Y. Grin, Type-I silicon clathrates containing lithium, Zeitschrift Für Kristallographie - Crystalline Materials. 232 (2017) 223–233. https://doi.org/10.1515/zkri-2016-1983.

[11] A. Ammar, C. Cros, M. Pouchard, N. Jaussaud, J.-M. Bassat, G. Villeneuve, M. Duttine, M. Ménétrier, E. Reny, On the clathrate form of elemental silicon, Si136: preparation and characterisation of NaxSi136 (x→0), Solid State Sciences. 6 (2004) 393–400. https://doi.org/10.1016/j.solidstatesciences.2004.02.006.

[12] A. Dopilka, J.M. Weller, A. Ovchinnikov, A. Childs, S. Bobev, X. Peng, C.K. Chan, Structural Origin of Reversible Li Insertion in Guest-Free, Type-II Silicon Clathrates, Adv Energy Sustain Res. 2 (2021) 2000114. https://doi.org/10.1002/aesr.202000114.

[13] S. Yamanaka, M. Komatsu, M. Tanaka, H. Sawa, K. Inumaru, High-Pressure Synthesis and Structural Characterization of the Type II Clathrate Compound $Na_{30.5}Si_{136}$ Encapsulating Two Sodium Atoms in the Same Silicon Polyhedral Cages, J. Am. Chem. Soc. 136 (2014) 7717–7725. https://doi.org/10.1021/ja502733e.

[14] L. Krishna, A.D. Martinez, L.L. Baranowski, N.P. Brawand, C.A. Koh, V. Stevanović, M.T. Lusk, E.S. Toberer, A.C. Tamboli, Group IV clathrates: synthesis, optoelectonic properties, and photovoltaic

applications, in: Physics, Simulation, and Photonic Engineering of Photovoltaic Devices III, SPIE, 2014: pp. 29–39. https://doi.org/10.1117/12.2040056.
[15] M. Imai, Semiconducting ternary Si clathrates, Jpn. J. Appl. Phys. 59 (2020) SF0804. https://doi.org/10.35848/1347-4065/ab69e1.
[16] K. Wei, Y. Dong, G.S. Nolas, Precursor routes to quaternary intermetallics: Synthesis, crystal structure, and physical properties of clathrate-II Cs8Na16Al24Si112, Journal of Solid State Chemistry. 237 (2016) 81–85. https://doi.org/10.1016/j.jssc.2016.01.020.
[17] M. Beekman, G.S. Nolas, Inorganic clathrate-II materials of group 14: synthetic routes and physical properties, J. Mater. Chem. 18 (2008) 842–851. https://doi.org/10.1039/B706808E.
[18] S. Bobev, S.C. Sevov, Clathrates of Group 14 with Alkali Metals: An Exploration, Journal of Solid State Chemistry. 153 (2000) 92–105. https://doi.org/10.1006/jssc.2000.8755.
[19] C.W. Myles, K. Biswas, E. Nenghabi, Rattling "guest" impurities in Si and Ge clathrate semiconductors, Physica B: Condensed Matter. 401–402 (2007) 695–698. https://doi.org/10.1016/j.physb.2007.09.054.
[20] S. Botti, J.A. Flores-Livas, M. Amsler, S. Goedecker, M.A.L. Marques, Low-energy silicon allotropes with strong absorption in the visible for photovoltaic applications, Phys. Rev. B. 86 (2012) 121204. https://doi.org/10.1103/PhysRevB.86.121204.
[21] A. Martinez, L. Krishna, L. Baranowski, M. Lusk, E. Toberer, A. Tamboli, Synthesis of Group IV Clathrates for Photovoltaics, Photovoltaics, IEEE Journal Of. 3 (2013) 1305–1310. https://doi.org/10.1109/JPHOTOV.2013.2276478.
[22] T. Kume, F. Ohashi, S. Nonomura, Group IV clathrates for photovoltaic applications, Jpn. J. Appl. Phys. 56 (2017) 05DA05. https://doi.org/10.7567/JJAP.56.05DA05.
[23] J. Wu, H. Gao, K. Xia, D. Xing, J. Sun, Silicon clathrates for photovoltaics predicted by a two-step crystal structure search, Appl. Phys. Lett. 111 (2017) 173904. https://doi.org/10.1063/1.5000444.
[24] K. Moriguchi, S. Munetoh, A. Shintani, First-principles study of $Si_{34-x}Ge_x$ clathrates: Direct wide-gap semiconductors in Si-Ge alloys, Phys. Rev. B. 62 (2000) 7138–7143. https://doi.org/10.1103/PhysRevB.62.7138.
[25] G.B. Adams, M. O'Keeffe, A.A. Demkov, O.F. Sankey, Y.-M. Huang, Wide-band-gap Si in open fourfold-coordinated clathrate structures, Phys. Rev. B. 49 (1994) 8048–8053. https://doi.org/10.1103/PhysRevB.49.8048.
[26] M. Beekman, K. Wei, G.S. Nolas, Clathrates and beyond: Low-density allotropy in crystalline silicon, Applied Physics Reviews. 3 (2016) 040804. https://doi.org/10.1063/1.4953165.
[27] M.A. Green, M.J. Keevers, Optical properties of intrinsic silicon at 300 K, Prog. Photovolt: Res. Appl. 3 (1995) 189–192. https://doi.org/10.1002/pip.4670030303.
[28] K.S. Chan, M.A. Miller, W. Liang, C. Ellis-Terrell, C.K. Chan, First principles and experimental studies of empty Si46 as anode materials for Li-ion batteries, Journal of Materials Research. 31 (2016) 3657–3665. https://doi.org/10.1557/jmr.2016.408.
[29] X. Li, K.X. Steirer, L. Krishna, C. Xiao, K. Fink, S. Santhanagopalan, Electrochemical Properties and Challenges of Type II Silicon Clathrate Anode in Sodium Ion Batteries, J. Electrochem. Soc. 166 (2019) A3051–A3058. https://doi.org/10.1149/2.1201913jes.
[30] F. Ohashi, Y. Iwai, A. Noguchi, T. Sugiyama, M. Hattori, T. Ogura, R. Himeno, T. Kume, T. Ban, S. Nonomura, Thin-film formation of Si clathrates on Si wafers, Journal of Physics and Chemistry of Solids. 75 (2014) 518–522. https://doi.org/10.1016/j.jpcs.2013.12.009.
[31] T. Narita, H. Ueno, T. Baba, T. Kume, T. Ban, T. Iida, H. Habuchi, H. Natsuhara, S. Nonomura, Preparation of NaSi thin films for the guest free Si clathrate thin films by heat resistance apparatus using NaSi target materials, Phys. Status Solidi (c). (2010) NA-NA. https://doi.org/10.1002/pssc.200982755.

[32] T. Kume, F. Ohashi, K. Sakai, A. Fukuyama, M. Imai, H. Udono, T. Ban, H. Habuchi, H. Suzuki, T. Ikari, S. Sasaki, S. Nonomura, Thin film of guest-free type-II silicon clathrate on Si (111) wafer, Thin Solid Films. 609 (2016). https://doi.org/10.1016/j.tsf.2016.03.056.
[33] T. Fix, R. Vollondat, A. Ameur, S. Roques, J.-L. Rehspringer, C. Chevalier, D. Muller, A. Slaoui, Silicon Clathrate Films for Photovoltaic Applications, J. Phys. Chem. C. 124 (2020) 14972–14977. https://doi.org/10.1021/acs.jpcc.0c02712.
[34] R. Kumar, Y. Hazama, F. Ohashi, H.S. Jha, T. Kume, A fabrication method for type-II Ge clathrate film by annealing of Ge film covered with Na layer, Thin Solid Films. 734 (2021) 138859. https://doi.org/10.1016/j.tsf.2021.138859.
[35] T. Kume, Y. Iwai, T. Sugiyama, F. Ohashi, T. Ban, S. Sasaki, S. Nonomura, NaSi and Si clathrate prepared on Si substrate, Physica Status Solidi (c). 10 (2013). https://doi.org/10.1002/pssc.201300397.
[36] H. Horie, T. Kikudome, K. Teramura, S. Yamanaka, Controlled thermal decomposition of NaSi to derive silicon clathrate compounds, Journal of Solid State Chemistry. 182 (2009) 129–135. https://doi.org/10.1016/j.jssc.2008.10.007.
[37] R. Himeno, T. Kume, F. Ohashi, T. Ban, S. Nonomura, Optical absorption properties of NaxSi136 clathrate studied by diffuse reflection spectroscopy, Journal of Alloys and Compounds. 574 (2013) 398–401. https://doi.org/10.1016/j.jallcom.2013.05.176.
[38] O.O. Kurakevych, T.A. Strobel, D.Y. Kim, T. Muramatsu, V.V. Struzhkin, Na-Si Clathrates Are High-Pressure Phases: A Melt-Based Route to Control Stoichiometry and Properties, Crystal Growth & Design. 13 (2013) 303–307. https://doi.org/10.1021/cg3017084.
[39] M.M. Makansi, C.H. Muendel, W.A. Selke, Determination of the Vapor Pressure of Sodium, J. Phys. Chem. 59 (1955) 40–42. https://doi.org/10.1021/j150523a012.
[40] L. Krishna, L.L. Baranowski, A.D. Martinez, C.A. Koh, P.C. Taylor, A.C. Tamboli, E.S. Toberer, Efficient route to phase selective synthesis of type II silicon clathrates with low sodium occupancy, CrystEngComm. 16 (2014) 3940–3949. https://doi.org/10.1039/C3CE42626B.
[41] S.L. Fang, L. Grigorian, P.C. Eklund, G. Dresselhaus, M.S. Dresselhaus, H. Kawaji, S. Yamanaka, Raman scattering from vibrational modes in Si46 clathrates, Phys. Rev. B. 57 (1998) 7686–7693. https://doi.org/10.1103/PhysRevB.57.7686.
[42] M. Menon, E. Richter, K.R. Subbaswamy, Structural and vibrational properties of Si clathrates in a generalized tight-binding molecular-dynamics scheme, Phys. Rev. B. 56 (1997) 12290–12295. https://doi.org/10.1103/PhysRevB.56.12290.
[43] R. Alben, D. Weaire, J.E. Smith, M.H. Brodsky, Vibrational properties of amorphous Si and Ge, Phys. Rev. B. 11 (1975) 2271–2296. https://doi.org/10.1103/PhysRevB.11.2271.
[44] J. Dong, O.F. Sankey, G. Kern, Theoretical study of the vibrational modes and their pressure dependence in the pure clathrate-II silicon framework, Phys. Rev. B. 60 (1999) 950–958. https://doi.org/10.1103/PhysRevB.60.950.
[45] Y. Guyot, B. Champagnon, E. Reny, C. Cros, M. Pouchard, P. Melinon, A. Perez, I. Gregora, Raman scattering of silicon clathrates, Phys. Rev. B. 57 (1998) R9475–R9477. https://doi.org/10.1103/PhysRevB.57.R9475.
[46] O.I. Barkalov, M.A. Kuzovnikov, I.A. Sholin, N.S. Orlov, Transformations of silicon clathrate Si136 under high hydrogen pressure up to 11 GPa, Solid State Communications. 340 (2021) 114492. https://doi.org/10.1016/j.ssc.2021.114492.
[47] R. Kumar, T. Maeda, Y. Hazama, F. Ohashi, H.S. Jha, T. Kume, Growth of Ge clathrate on sapphire and optical properties, Jpn. J. Appl. Phys. 59 (2020) SFFC05. https://doi.org/10.35848/1347-4065/ab6e0a.

[48] P. Mélinon, B. Prevel, V. Dupuis, A. Perez, B. Champagnon, Y. Guyot, M. Boudeulle, M. Pellarin, J. Lermé, M. Broyer, Cluster assembled thin films of covalent materials, Zeitschrift Fur Physik D-Atoms Molecules and Clusters. 40 (1997) 554–558. https://doi.org/10.1007/s004600050276.
[49] W.K. Schenken, Y. Liu, L. Krishna, A.A.A. Majid, C.A. Koh, P.C. Taylor, R.T. Collins, Electron paramagnetic resonance study of type-II silicon clathrate with low sodium guest concentration, Phys. Rev. B. 101 (2020) 245204. https://doi.org/10.1103/PhysRevB.101.245204.
[50] Y. Liu, W.K. Schenken, L. Krishna, A.A.A. Majid, T.E. Furtak, M. Walker, C.A. Koh, P.C. Taylor, R.T. Collins, Synthesis and characterization of type II silicon clathrate films with low Na concentration, Applied Physics Reviews. 8 (2021) 041408. https://doi.org/10.1063/5.0062723.
[51] M. Yamaga, T. Kishita, T. Kume, K. Uehara, M. Nomura, F. Ohashi, T. Ban, S. Nonomura, Electron-Spin Resonance of Type II Si-Clathrate Thin Film for New Solar Cell Material, (2016) 213–219. https://doi.org/10.1007/978-3-319-45677-5_26.
[52] O.A. Jaramillo-Quintero, M.E. Rincón, G. Vásquez-García, P.K. Nair, Influence of the electron buffer layer on the photovoltaic performance of planar $Sb_2(S_xSe_{1-x})_3$ solar cells, Prog Photovolt Res Appl. 26 (2018) 709–717. https://doi.org/10.1002/pip.3007.

Figure captions

Fig. 1. Photographs of the experimental setup used for a) the synthesis of the Zintl precursor film b) for the thermal decomposition of the precursor into the silicon clathrates film.

Fig. 2. Nature of the films obtained depending on the temperature of the first annealing step.

Fig. 3. XRD patterns for the a) SiCL-I b) SiCL-II films. The red cercles refers to Na_1Si_{136} (JCPDS 01-089-5535), the blue triangles to Na_8Si_{46} (JCPDS 01-089-5534) and the black squares to diamond Silicon (JCPDS 00-027-1402). Raman spectra obtained with a 532nm laser at 1.1 mW using a 2400 $g.mm^{-1}$ grating with a 50 µm slit for c) SiCL-I d) SiCL-II films.

Fig. 4. a) Absorption coefficients α of the SiCL films and Silicon versus the photon energy E_{Ph} in the 210-800 nm range. b) Tauc Plot for SiCL-II film assuming a b) direct c) indirect optical band gap.

Fig. 5. TEM observations of SiCL-I (on the left) and SiCL-II (on the right) from a suspension in ethanol.

Fig. 6. a) Variation of the Contact Potential Difference (CPD) measured on the Silicon Clathrates samples during cycle between illumination by halogen visible light and dark. b) Surface Photovoltage (SPV) of the Silicon Clathrates samples according to the illumination delivered by the halogen visible light.

Fig.7. Surface Photovoltage Spectroscopy of the Silicon Clathrates samples and Silicon by normalizing the SPV by the photon flux versus the wavelength of the light.

Fig. 8. XRD patterns for the a) SiCL-II films submitted to 200°C and 250°C with a force of 2kN b) SiCL-II films submitted to 2 and 4 kN at a temperature of 250°C. Purple asterisks are for the $NaSi_6$ (JCPDS 04-020-2170) c) Raman Spectra obtained with a 532nm laser before and after press annealing of a SiCL-II sample at 250°C for a force of 4 kN during 30 minutes.